IEEE Photonics Journal
An IEEE Photonics Society Publication

A Dimmable OFDM Scheme With Dynamic Subcarrier Activation for VLC

Volume 12, Number 1, February 2020

Congcong Wang
Yang Yang
Julian Cheng
Caili Guo
Chunyan Feng

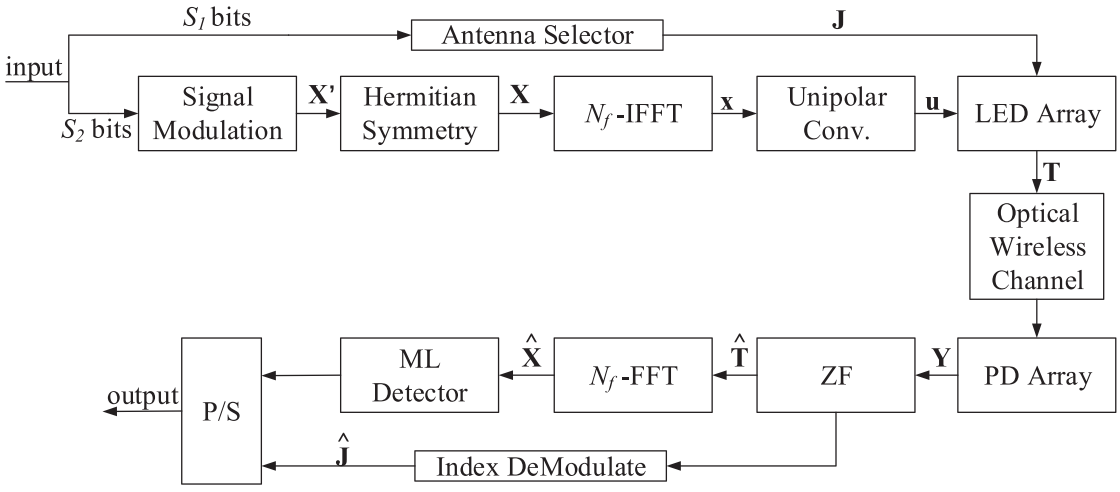

DOI: 10.1109/JPHOT.2019.2958272

A Dimmable OFDM Scheme With Dynamic Subcarrier Activation for VLC

Congcong Wang,[1] Yang Yang,[1] Julian Cheng,[2] Caili Guo,[3] and Chunyan Feng [1]

[1]Beijing Key Laboratory of Network System Architecture and Convergence, School of Information and Communication Engineering, Beijing University of Posts and Telecommunications, Beijing 100876, China
[2]The University of British Columbia, Kelowna, BC V6T 1Z4, Canada
[3]Beijing Laboratory of Advanced Information Networks, School of Information and Communication Engineering, Beijing University of Posts and Telecommunications, Beijing 100876, China

DOI:10.1109/JPHOT.2019.2958272

Manuscript received October 17, 2019; revised November 28, 2019; accepted December 3, 2019. Date of publication December 9, 2019; date of current version January 7, 2020. This work was supported in part by the National Science Foundation of China under Grant 61871047 and in part by the China Postdoctoral Science Foundation under Grant 2018M641278. Corresponding author: Caili Guo (e-mail: guocaili@bupt.edu.cn).

Abstract: Dimmable optical orthogonal frequency division multiplexing (D-OFDM) is challenging to design for visible light communications, due to the high peak-to-average power ratio (PAPR) of OFDM signals and limited dynamic range of LEDs. Current D-OFDM schemes focused on the time domain and spatial domain designs of OFDM signals. This paper proposes a novel dynamic subcarrier activation based OFDM (DSA-OFDM) scheme. In DSA-OFDM, the number of activated subcarriers, as well as the signal's DC bias and the number of activated LEDs, is adjusted to provide both flexible dimming control and reliable communication. A generalized index modulation in both spatial domain and frequency domain is designed to select the activated subcarriers and activated LEDs. To show the influence of frequency domain design analytically, the closed-form expressions of the PAPR and the clipping noise of the DSA-OFDM signals are derived, and the optimized signal form is obtained accordingly. Simulation and numerical results show that the proposed scheme can outperform conventional dimming control schemes at various illumination levels in terms of the bit-error rate performance.

Index Terms: Dimming control, orthogonal frequency division multiplexing, peak-to-average power ratio, visible light communication.

1. Introduction

Visible light communication (VLC) has emerged as a promising short range wireless access technology, and it is predicted to offer an excess of 100 Gb/s data rate in the near future [1]. Light-emitting diodes (LEDs) are often deployed as transmitters in VLC systems, which can provide reliable optical signal and achieve high energy efficiency. Besides, VLC has wide license-free bandwidth to support high data rate transmission [2]. The advantage of non-electromagnetic interference makes this technology particularly suitable for co-existing with conventional radio frequency (RF) based access technologies [3].

Optical orthogonal frequency division multiplexing (O-OFDM) is deemed as a more suitable modulation scheme for VLC than the single-carrier schemes, since O-OFDM suffers less from inter-symbol interference and has high spectral efficiency [4]. In order to maintain the signals real-valued

and non-negative, several O-OFDM schemes have been proposed, such as direct current biased O-OFDM (DCO-OFDM) [5] and asymmetrically clipped O-OFDM [6]. Besides, to support dimming control, several types of dimmable optical OFDM (D-OFDM) schemes have been proposed. Analogue dimming (AD) schemes, such as enhanced DCO-OFDM [7], achieve dimming control by varying the DC bias of the transmit signals. However, the dimming range of AD needs to be small to avoid excessive clipping noise caused by the high peak-to-average power ratio (PAPR) of OFDM signals. To avoid high PAPR, digital dimming (DD) schemes achieve dimming control by adjusting the duty cycle of digital signals. In [8], the authors proposed a composite signal form of OFDM and pulse width modulation (PWM) for high-speed communication, where the duty cycle of PWM was used to achieve dimming control. In addition, spatial dimming (SD) was proposed in [9], and it achieves dimming control by adjusting the number of activated LEDs in an LED array. In this way, the DC bias of OFDM signals is always equal to the middle of the dynamic range of LEDs, so that a relatively high PAPR can be tolerated. However, the data rate of DD is constrained by the duty cycle of the PWM signal, while the dimming range and dimming accuracy of SD is constrained by the total number of LEDs in the LED array. Recently, a hybrid dimmable OFDM (HD-OFDM) scheme that combines AD and SD was proposed in [10] to achieve the advantages of the both. However, when the dimming level is sufficiently high, all the LEDs should be activated to satisfy the required dimming level, and the high PAPR issue of OFDM signals still degrades the performance of HD-OFDM.

Different from the RF based PAPR reduction scheme, the optical power constraint of OFDM signals should also be considered in the PAPR reduction schemes for VLC. This is particularly important for D-OFDM schemes, in which the optical power changes dynamically. This is because the optical power is mainly determined by the DC bias, while the DC bias has a direct impact on the PAPR of D-OFDM signals. However, the conventional PAPR reduction methods in RF [11] and VLC [12]–[14] do not take the optical power constraints into consideration. This motivates us to combine the PAPR reduction technology with dimming control in D-OFDM for VLC. The existing studies have focused on the time domain design of OFDM signals, while the frequency domain design also matters for a D-OFDM scheme. More specifically, the number of activated subcarriers can significantly affect the PAPR of OFDM signals [15], [16], thus further affecting the performance of a D-OFDM scheme. Hence, even though the frequency design of OFDM signals may not directly determine the optical power, it is necessary to be considered in a D-OFDM scheme.

The main contribution of this paper is to propose a novel dynamic subcarrier activation based OFDM (DSA-OFDM) scheme for VLC to achieve flexible dimming control and reliable communication. Since the dynamic subcarrier activation is based on frequency domain design, DSA-OFDM can be combined with existing D-OFDM schemes that focused on the time and spatial design of OFDM signals. Therefore, in DSA-OFDM, the number of activated subcarriers, as well as the signal's DC bias and the number of activated LEDs, is adjusted for a target illumination level. Since only parts of subcarriers and LEDs are activated, a generalized index modulation in both spatial and frequency domains is employed to select the indices of activated subcarriers and the indices of activated LEDs. To investigate the performance of DSA-OFDM, we derive the closed-form expressions of the PAPR and the clipping noise of DSA-OFDM signals, and then obtain the optimized signal form of DSA-OFDM accordingly. Simulation and numerical results verify that the proposed DSA-OFDM can outperform conventional dimming control schemes without frequency domain design in terms of BER performance at various illumination levels.

The remainder of this paper is organized as follows. In Section 2, we introduce a typical dimmable multiple-imput multiple-output (MIMO) OFDM based VLC system model. Section 3 presents the detail of the proposed DSA-OFDM. In Section 4, simulation and numerical results are presented and analyzed. Finally, we draw some important conclusions in Section 5.

2. System Model

This section introduces a typical dimmable MIMO-OFDM based VLC system. As shown in Fig. 1, we present the block diagram of a typical dimmable MIMO-OFDM based VLC system with N_T LEDs and N_R photo-detectors (PDs). Let N_A, $1 \leq N_A \leq N_T$ be the number of activated LEDs turned on at

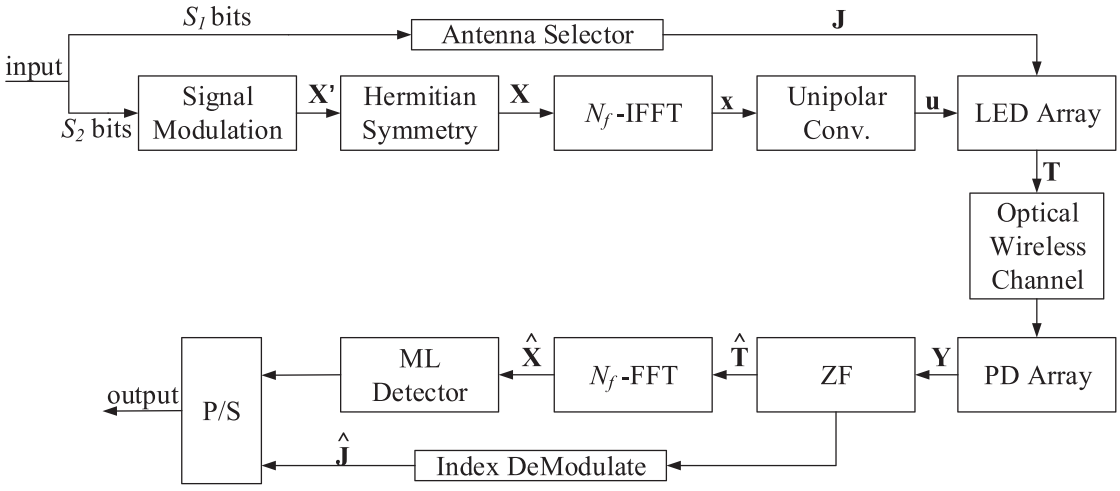

Fig. 1. Block diagram of a typical dimmable MIMO-OFDM based VLC system.

each time slot. In addition, information are transmitted by both the OFDM signals and the indices of the activated LEDs. Here, we assume S_1 bits are fed into the antenna selector to active N_A out of N_T LEDs, while S_2 bits are modulated according to certain constellation such as pulse amplitude modulation or quadratic amplitude modulation (QAM).

As shown in Fig. 1, antenna selector generates an N_T-length spatial vector $\mathbf{J} = [j^1, j^2, \ldots, j^{N_T}]^{\mathrm{T}}$ to determine the indices of activated LEDs at a time slot, where $j^i \in \{0, 1\}, 1 \leq i \leq N_T$. Note that $j^i = 1$ represents that the ith LED is activated and $j^i = 0$ represents that the ith LED is idle. There are $\binom{N_T}{N_A}$ possibile LED activation patterns, and thus $N_l = \lfloor \log_2 \binom{N_T}{N_A} \rfloor$ bits can be conveyed by each activation pattern.

To maintain the time-domain OFDM signals real, Hermitian symmetry is imposed on the OFDM block as

$$\begin{cases} X_k = X^*_{N_f - k}, & k = 1, 2, \ldots, N_f/2 - 1 \\ X_0 = X_{N_f/2} = 0 \end{cases} \tag{1}$$

where $(\cdot)^*$ denotes conjugation operator, N_f is the size of the inverse fast fourier transformation (IFFT), and X_k is the frequency-domain OFDM signal on the kth subcarrier. Thus the time-domain OFDM signal is obtained by IFFT as

$$x_n = \frac{1}{\sqrt{N_f}} \sum_{k=0}^{N_f - 1} X_k \exp\left(j \frac{2\pi}{N_f} nk \right) \tag{2}$$

for $n = 0, 1, \ldots, N_f - 1$. By a pre-equalization circuit at transmitter, the high-frequency power fading characteristics of the LEDs can be compensated [17] and in this work, we assume that a pre-equalization circuit [18], [19] is employed. Therefore, the frequency transmission characteristics of the LEDs are assumed to be flat. Moreover, to maintain the time-domain OFDM signals non-negative, the system uses a DC bias B_{L}. In addition, a scaling factor α is used to control the electrical power of OFDM signals, and thus the unipolar conversion can be expressed as $u_n = \alpha x_n + B_{\mathrm{L}}$. Without loss of generality, a nonlinear piecewise polynomial function is used to represent the LED transfer function [20], and thus the clipped signal t_n can be expressed as

$$t_n = \Xi(u_n) = \begin{cases} I_{\mathrm{L}}, & u_n < I_{\mathrm{L}} \\ I_3 u_n^3 + I_2 u_n^2 + I_1 u_n + I_0, & I_{\mathrm{L}} \leq u_n < I_{\mathrm{H}} \\ I_{\mathrm{H}}, & I_{\mathrm{H}} \leq u_n \end{cases} \tag{3}$$

where I_3, I_2, I_1 and I_0 are the third-order nonlinearity coefficient, the second-order nonlinearity coefficient, the linear coefficient and the constant term, respectively. In line with [20], we set $I_3 = -1.6461$, $I_2 = 2.7160$, $I_1 = -0.4938$ and $I_0 = 0.0239$ in our system. Since both the DC bias and the scaling factor of the transmit signals can be adjusted for dimming control, the normalized illumination level can be expressed as

$$\eta = \frac{N_A}{N_T}\eta_e \times 100\% \tag{4}$$

where η_e is the illumination level of each LED. The received signal vector $\mathbf{Y}_n = [y_n^1, y_n^2, \ldots, y_n^{N_R}]^{\mathrm{T}}$ can be expressed as

$$\mathbf{Y}_n = \mathbf{H}\mathbf{T}_n + \mathbf{W}_n \tag{5}$$

for $n = 0, 1, \ldots, N_f - 1$, where $\mathbf{T}_n = \mathbf{J}_n t_n$ is the transmitted signal vector, $\mathbf{J}_n$ is the index matrix of the LED activation pattern, and $\mathbf{W}_n$ denotes the additive white Gaussian noise (AWGN) vector whose elements w_n^i, $i = 1, 2, \ldots, N_R$ follow Gaussian independent, identically distribution (i.i.d.) with mean zero and variance σ_w^2. In (5), $\mathbf{H} \in \mathbb{R}^{N_R \times N_T}$ is the channel matrix, whose (i, j)-th element $h_{i,j}$ is the channel gain between the j-th LED and the i-th PD. Note that the optical signal can be transmitted by either LOS links or non-LOS links. However, since more than 95% of the light collected by optical receiver is from the LOS links [21] and the root mean delay between LOS links and non-LOS links is typically on the order of nano seconds [10], only the LOS optical propagation link with flat channel is considered in this work [22], [23]. The channel gain of a LOS link between the j-th LED and the i-th PD can be expressed as

$$h_{i,j} = \begin{cases} \dfrac{(m+1)A}{2\pi d_{i,j}^2} g(\psi)\cos^m(\phi)\cos(\psi), & 0 < \psi < \Psi_{1/2} \\ 0, & \psi > \Psi_{1/2} \end{cases} \tag{6}$$

where m is the Lambert order defined as $m = -\frac{\ln 2}{\ln(\cos \Phi_{1/2})}$ and $\Phi_{1/2}$ is the transmitter semiangle (at half power) [10]. In addition, A is the detector area, $d_{i,j}$ is the distance between the j-th LED and the i-th PD, ϕ is the angle of irradiance, ψ is the angle of incidence, $\Psi_{1/2}$ is the receiver field of vision (FOV) semiangle and $g(\psi)$ denotes the gain of optical concentrator which can be denoted as

$$g(\psi) = \begin{cases} \dfrac{{n_r}^2}{\sin^2 \Psi_{1/2}}, & 0 < \psi < \Psi_{1/2} \\ 0, & \psi \geq \Psi_{1/2} \end{cases} \tag{7}$$

where n_r is the refractive index.

In this work, since VLC channel estimation method such as [24] can closely estimate the analytical channel gain, we assume that the channel state information is perfectly known at the receiver for simplicity. At the receiver, the indices of activated LEDs need to be detected first, so that the VLC signals can be properly demodulated. To achieve this goal, zero-forcing (ZF) is used to estimate the indices of the activated LEDs, and it yields an estimate of $\mathbf{T}_n$ as

$$\widehat{\mathbf{T}}_n = \mathbf{H}^{\dagger}\mathbf{Y}_n \tag{8}$$

for $n = 0, 1, \ldots, N_f - 1$, where $\widehat{\mathbf{T}}_n \in \mathbb{C}^{N_T \times 1}$ is the estimated matrix of $\mathbf{T}_n$, $\mathbf{H}^{\dagger}$ denotes the generalized inverse of the channel matrix $\mathbf{H}$. After this operation, the receiver sorts the N_T estimated signals of $\widehat{\mathbf{T}}_n$ and selects the first N_A signals having larger values into set $\mathbb{F}$. In this way, the estimated spatial vector $\widehat{\mathbf{J}}_n$ can be recovered according to the same lookup table used at the transmitter. Meanwhile, $\widehat{t_n}$ be obtained by calculating the average value of the N_A elements in set $\mathbb{F}$, and then $\widehat{t_n}$ is applied to recover $\widehat{x_n}$ according to (3). Next, $\widehat{x_n}$ is converted to frequency-domain OFDM signals $\widehat{X_k}$ according to FFT

$$\widehat{X_k} = \frac{1}{\sqrt{N_f}} \sum_{n=0}^{N_f-1} \widehat{x_n} \exp\left(-\frac{j2\pi nk}{N_f}\right) \tag{9}$$

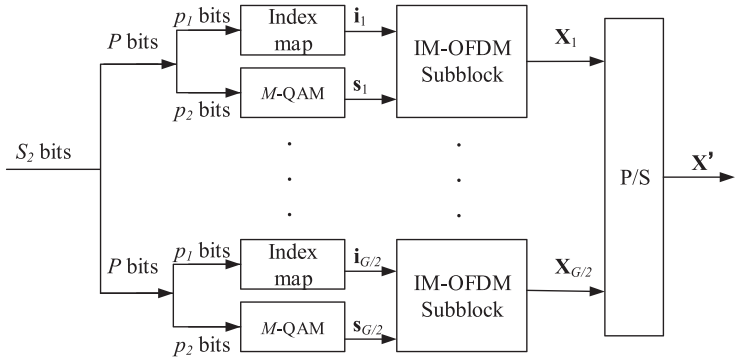

Fig. 2. Block diagram of OFDM signal modulation in DSA-OFDM.

for $k = 0, 1, \ldots, N_f - 1$, and then $\widehat{X}_k$ can be decoded by a maximum likelihood (ML) detector.

3. DSA-OFDM

Even though the performance of D-OFDM schemes can be enhanced by simultaneously adjusting the number of activated LEDs and the DC bias, their performance is still limited by the notorious high PAPR issue. The composite envelope of OFDM is a superposition of multiple subcarrier signals. According to the central limit theorem, when the number of subcarriers is large enough, the time domain OFDM signals can be approximated as the Gaussian i.i.d. by a central limit theorem (CLT) [25]. Therefore, the OFDM signals have larger PAPR than the signals in single carrier systems. Generally, the PAPR of OFDM signals increases with the number of activated subcarriers [26]. Index modulation assisted OFDM [27] is a novel modulation scheme where only parts subcarriers are activated so that this scheme can result in low PAPR. Based on these observations, a novel DSA-OFDM scheme that dynamically adjusts the number of activated subcarriers for dimming control is proposed.

3.1 Design of DSA-OFDM

In DSA-OFDM, the index modulation in both spatial and frequency domains is designed to select the activated LEDs and activated subcarriers, and thus the information is transmitted by constellation symbols, the indices of activated LEDs and the indices of activated subcarriers. The block diagram of OFDM signal modulation in DSA-OFDM is shown in Fig. 2.

In DSA-OFDM, the N_f subcarriers are divided into G subblocks, and each subblock contains $N = N_f/G$ subcarriers. Due to the Hermitian symmetry, we only consider the first half OFDM subcarriers. For each subblock g, $1 \le g \le G/2$, only K out of N subcarriers are activated for the transmission while the rest $N - K$ subcarriers are set to zero. For each subblock, there are $\binom{N}{K}$ possible activation patterns, and thus $\lfloor \log_2 \binom{N}{K} \rfloor$ bits can be transmitted by the indices of subcarriers.

As shown in Fig. 2, S_2 bits are first converted into $G/2$ bit sequences, where each sequence has $p_1 + p_2$ bits. For the g-th sequence, $p_1 = \lfloor \log_2 \binom{N}{K} \rfloor$ bits are mapped to a N-length vector $\mathbf{i}_g = [i_g^1, i_g^2, \ldots, i_g^N]^{\mathrm{T}}$, $i_g^{n_1} \in \{0, 1\}$, $n_1 = 1, 2, \ldots, N$. Furthermore, the vector $\mathbf{i}_g$ is used to select the indices of activated subcarriers for the g-th subblock, where $i_g^{n_1} = 1$ indicates that the n_1th subcarrier is activated and $i_g^{n_1} = 0$ indicates that the n_1th subcarrier is idle. In particular, both the look up table method and the combinatorial method [28] can be used to map p_1 bits into the vector $\mathbf{i}_g$. Since the value of p_1 is small, the look up table method is used in this work. For instance, a lookup table of the subcarrier selector for $N = 4$ and $K = 2$ is presented in Table 1.

Meanwhile, the remaining $p_2 = K \log_2 M$ bits are mapped to a K M-QAM symbols. A K-length vector $\mathbf{s}_g = [s_g^1, s_g^2, \ldots, s_g^K]^{\mathrm{T}}$, $s_g^k \in \mathcal{S}$, $k = 1, 2, \ldots, K$ is imposed to denote the M-QAM symbols for

TABLE 1
A Lookup Table of Subcarrier Selector for N=4 and K=2

p_1-Bits	Indices of activated subcarriers	$\mathbf{i}_g$
[0 0]	(1,2)	[1 1 0 0]
[0 1]	(2,3)	[0 1 1 0]
[1 0]	(3,4)	[0 0 1 1]
[1 1]	(1,3)	[1 0 1 0]

subblock g, where $\mathcal{S}$ is the set of all possible M-QAM symbols. For the g-th subblock, the kth elements of $\mathbf{s}_g$ are mapped to the kth activated subcarriers according to the vector $\mathbf{i}_g$. Then, all of the DSA-OFDM subblocks are converted into $\mathbf{X}' \in \mathbb{C}^{(N_f/2-1)\times 1}$, which is given as

$$\mathbf{X}' = \left[\mathbf{X}_1\ \mathbf{X}_2\ \cdots\ \mathbf{X}_{G/2}\right]^{\mathrm{T}} = \left[X_0, X_1, \ldots, X_{N_f/2-1}\right]^{\mathrm{T}}. \tag{10}$$

Imposing Hermitian symmetry, we can express the frequency-domain DSA-OFDM signals as $\mathbf{X} = [0, X_1, \ldots, X_{N_f/2-1}, 0, X^*_{N_f/2-1}, \ldots, X^*_1]^{\mathrm{T}}$. Then, $\mathbf{X}$ is converted to time-domain signals $x_n, n = 0, 1, \ldots, N_f$ according to (2).

At the receiver, the detector of DSA-OFDM needs to extract the indices of activated subcarriers from the OFDM signals. To this end, we first obtain the estimated vector of frequency-domain OFDM signals $\widehat{\mathbf{X}} = [\widehat{X}_0, \widehat{X}_1, \ldots, \widehat{X}_{N_f-1}]$ from FFT, and then the estimated vector $\widehat{\mathbf{X}}$ is converted into G subblocks. For the g-th subblock, we have $\widehat{\mathbf{X}}_g = [\widehat{X}_{N(g-1)}, \widehat{X}_{N(g-1)+1}, \ldots, \widehat{X}_{N(g-1)+N-1}]$. Furthermore, the ML detector is used to detect the indices of activated subcarriers and the transmitted signals [28]. The detection implementation can be expressed as

$$\left(\widehat{\mathbf{i}}_g, \widehat{\mathbf{s}}_g\right)_{\mathrm{ML}} = \arg\min_{\mathbf{i}_g, \mathbf{s}_g} \sum_{k=1}^{K} \left|\widehat{\mathbf{X}}_g - \mathbf{X}_g\right|^2 \tag{11}$$

where $\widehat{\mathbf{i}}_g$ and $\widehat{\mathbf{s}}_g$ denote the estimated vector of $\mathbf{i}_g$ and $\mathbf{s}_g$, respectively, $\widehat{\mathbf{X}}_g \in \mathcal{A}$ is the estimated vector of $\mathbf{X}_g$, where $\mathcal{A}$ is the set of all possible combinations of $\mathbf{i}_g$ and $\mathbf{s}_g$. After this operation, $\widehat{\mathbf{i}}_g$ is demapped into p_1 bits according to the lookup table of subcarrier selector, and then the demodulation of the constellation symbols can be conducted directly once the indices of activated LEDs and activated subcarriers are obtained. Furthermore, since the total decoding complexity of ML detector in OFDM with index modulation is considerably higher than that of classical OFDM, a simple low-cost GD detector [29] is also employed in DSA-OFDM. Unlike the ML detector, the GD detector performs a two-stage search to find the indices of activated subcarriers and QAM symbols. In contrast, since the number of bits transmitted by N OFDM subcarriers is $P_{\mathrm{HD}} = N\log_2 M$ in HD-OFDM, the decoding complexity of N subcarriers in HD-OFDM is $\mathcal{O}(N2^{P_{\mathrm{HD}}/N})$.

3.2 PAPR Analysis

The PAPR of DSA-OFDM signals before clipping is analyzed in this subsection, and it is defined as

$$\mathrm{PAPR} = \frac{\max_{0\le n\le N_f-1}\left\{u_n{}^2\right\}}{\mathrm{E}\left[u_n{}^2\right]} \tag{12}$$

where $\mathrm{E}[u_n^2]$ corresponds to the average power of the transmitted signals u_n.

Without loss of generality, the complex symbol $X_k, k = 0, 1, \ldots, N_f - 1$ are assumed to be statistically i.i.d. random variables having zero mean and variance $\sigma_x^2 = \mathrm{E}[X_k^2]$ [30]. The time domain OFDM signals $x_n, n = 0, 1, \ldots, N_f - 1$ are obtained by the IFFT of N_f i.i.d. discrete random variables X_k. Since only a subset of subcarriers is activated in DSA-OFDM, $x_n, n = 0, 1, \ldots, N_f - 1$ asymptotically becomes Gaussian distributed with zero mean and variance $(\frac{K}{N}\sigma_x)^2$ by a central limit theorem [25]. Besides, the correlation among $x_n, n = 0, 1, \ldots, N_f - 1$ tends to be zero for large

N_f [30]. Moreover, u_n is obtained by the linear unipolar conversion of x_n, i.e. $u_n = \alpha x_n + B_L$, and thus $u_n, n = 0, 1, \ldots, N_f - 1$ are asymptotically i.i.d. Gaussian variables with mean $E(u_n) = B_L$ and variance $\sigma_u^2 = (\frac{K}{N}\alpha\sigma_x)^2$ [31]. Then the complementary cumulative distribution function (CCDF) of the PAPR can be expressed as

$$\begin{aligned}
\text{CCDF}(\zeta) &= 1 - \Pr\{\text{PAPR} \le \zeta\} \\
&= 1 - \Pr\left\{\max_{0\le n\le N_f-1}\{u_n^2\} \le \mathrm{E}\left[u_n^2\right]\zeta\right\} \\
&= 1 - \Pr\left\{u_n \le \sqrt{\mathrm{E}\left[u_n^2\right]\zeta}, n = 0, 1, \ldots, N_f - 1\right\} \\
&= 1 - \prod_{n=0}^{N_f-1} \Pr\left\{u_n \le \sqrt{\mathrm{E}\left[u_n^2\right]\zeta}\right\} \\
&= 1 - \left\{\Phi\left(\frac{\sqrt{\zeta\left[\left(\frac{K}{N}\sigma_x\alpha\right)^2 + B_L^2\right]} - B_L}{\frac{K}{N}\sigma_x\alpha}\right)\right\}^{N_f}
\end{aligned} \tag{13}$$

where $\Phi(x) = \int_{-\infty}^{x} \frac{1}{\sqrt{2\pi}} \exp(-\frac{t^2}{2})\mathrm{d}t$, and for $0 \le \zeta \le 1$, there is $\zeta[(\frac{K}{N}\sigma_x\alpha)^2 + {B_L}^2] - B_L \ge 0$. Note that the variance $\sigma_u^2 = \mathrm{E}[u_n^2] - [\mathrm{E}(u_n)]^2$, and thus $\mathrm{E}[u_n^2] = (\frac{K}{N}\alpha\sigma_x)^2 + {B_L}^2$. We can observe that the CCDF of PAPR is independent of the modulation order of signals, but it is closely related to the value of K/N. Specifically, for fixed values of ζ and B_L, the PAPR of OFDM signals increases with K/N.

3.3 Clipping Noise Analysis

Based on the analysis of the PAPR of DSA-OFDM signals, the clipping noise of DSA-OFDM signals is analyzed in this subsection. Since the pre-clipped signal u_n is approximately Gaussian with mean B_L and variance $\sigma_u^2 = \frac{K}{N}\alpha^2\sigma_x^2$, the clipped signal t_n can be modeled according to the Busggang theorem [20] as

$$t_n = \gamma u_n + z_n \tag{14}$$

where z_n denotes the clipping noise, which is uncorrelated with u_n, and γ is an attenuation factor. We define $\mu \triangleq \frac{I_L - B_L}{\sigma_u}$, $\nu \triangleq \frac{I_H - B_L}{\sigma_u}$, and the attenuation factor is given by

$$\gamma = \frac{\mathrm{cov}[u_n, t_n]}{\sigma_u^2} = \Phi(\nu) - \Phi(\mu) \tag{15}$$

where $\sigma_u > 0$. Furthermore, the variance of the clipping noise z_n can be expressed as

$$\begin{aligned}
{\sigma_z}^2 &= \mathrm{E}\left[(t_n - \gamma u_n)^2\right] - \mathrm{E}[t_n - \gamma u_n]^2 \\
&= \mathrm{E}\left[t_n^2\right] - \gamma^2\sigma_u^2 - \mathrm{E}[t_n]^2.
\end{aligned} \tag{16}$$

In (16), $\mathrm{E}[t_n^2]$ and $\mathrm{E}[t_n]$ can be calculated as

$$\begin{aligned}
\mathrm{E}\left[t_n^2\right] &= \int_{-\infty}^{\mu} I_L^2\phi(t)dt + \int_{\mu}^{\nu} u_n^2\phi(t)dt + \int_{\nu}^{+\infty} I_H^2\phi(t)dt \\
&= \Phi(\mu)\left(I_L^2 - \sigma_u^2 - B_L^2\right) + \Phi(\nu)\left(\sigma_u^2 + B_L^2 - I_H^2\right) + I_H^2 - \frac{\sigma_u}{\sqrt{2\pi}}(I_H - B_L)\exp\left(-\frac{\nu^2}{2}\right) \\
&\quad + \frac{\sigma_u}{\sqrt{2\pi}}(I_L - B_L)\exp\left(-\frac{\mu^2}{2}\right) - \frac{2B_L\sigma_u}{\sqrt{2\pi}}\left[\exp\left(-\frac{\nu^2}{2}\right) - \exp\left(-\frac{\mu^2}{2}\right)\right]
\end{aligned} \tag{17}$$

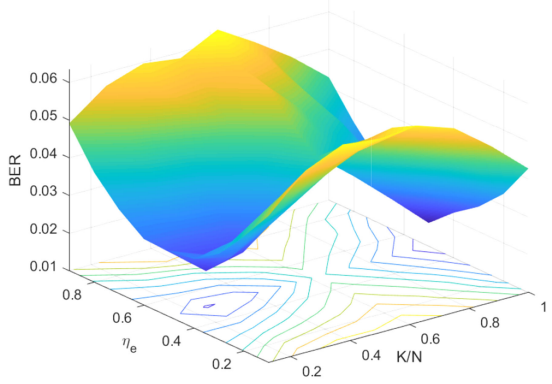

Fig. 3. The BER performance of an activated LED with different values of η_e and K/N at a fixed spectral efficiency. The simulation parameters are shown in Table III, except that N is set to 8.

$$\begin{aligned}\mathrm{E}[t_n] &= \int_{-\infty}^{\nu} I_{\mathrm{L}}\phi(t)dt + \int_{\mu}^{\nu} u_n\phi(t)dt + \int_{\nu}^{+\infty} I_{\mathrm{H}}\phi(t)dt \\ &= \Phi(\mu)(I_{\mathrm{L}} - B_{\mathrm{L}}) + \Phi(\nu)(B_{\mathrm{L}} - I_{\mathrm{H}}) + I_{\mathrm{H}} - \frac{\sigma_u}{\sqrt{2\pi}}\left[\exp\left(-\frac{\nu^2}{2}\right) - \exp\left(-\frac{\mu^2}{2}\right)\right] \end{aligned} \tag{18}$$

where $\phi(x) = \frac{1}{\sqrt{2\pi}}\exp(-\frac{x^2}{2})$. To simplify the analysis, we assume that $\sigma_x^2 = 1$. According to (16)–(18), we can observe that there is a close relationship between σ_z^2 and σ_u^2. More specifically, σ_u^2 increases with K/N.

3.4 Performance Optimization

In DSA-OFDM, the information is transmitted not only by the constellation symbols but also by the indices of activated LEDs and the indices of activated subcarriers. Since there are only $(N-1)$ subcarriers in the first subblock, the first subblock is unavailable for subcarrier index modulation. Therefore, only $(\frac{G}{2}-1)$ subblocks are used for subcarrier index modulation and constellation symbol transmission [32]. Specifically, the spectral efficiency of DSA-OFDM ξ can be expressed as

$$\xi = \frac{N_f - 2N}{2NN_f}\left(K\log_2(M) + \left\lfloor \log_2\binom{N}{K}\right\rfloor\right) + \left\lfloor \log_2\binom{N_T}{N_A}\right\rfloor \text{ bit/s/Hz}. \tag{19}$$

Figure 3 shows the BER performance of an activated LED having different values of η_e and K/N at a fixed spectral efficiency. We can observe that for a fixed K/N, the system has the best BER performance at the mid-level illumination level. This is because that for a given K/N, the DC bias of the OFDM signals increases with η_e. When η_e is small, the resulting low DC bias makes the OFDM signals prone to be clipped by the lower bound of the dynamic range of LEDs. In contrast, when η_e is large, the OFDM signals are prone to be clipped by the upper bound of the dynamic range of LEDs. On the other hand, for a given η_e, the BER tends to increase as the K/N changes from 0 to 0.6, while it decreases as the K/N changes from 0.6 to 1. Note that the number of activated LEDs N_A can also be varied in DSA-OFDM, and thus there is a tradeoff between N_A and K/N, which is important for the system performance optimization.

Furthermore, the SNR of DSA-OFDM symbols is the ratio between the power of the undistorted part of the signal and the noise power, and it can be expressed as

$$\mathrm{SNR} = \frac{N_A\alpha^2 K/N}{\sigma_z^2 + \sigma_w^2 + \sigma_{\mathrm{index}}^2} \tag{20}$$

TABLE 2
Simulation Parameters

Name of Parameters	Values
Turn-on current, I_{L}	0.1 A
Maximum allowed current, I_{H}	0.6 A
Number of LEDs, N_T	4
Number of PDs, N_R	4
Number of subcarriers, N	4
Number of subblock, G	64
Semiangle at half power, $\Phi_{1/2}$	80°
Receiver FOV semiangle, $\Psi_{1/2}$	80°

where σ^2_{index} is the equivalent additive noise resulted from the detection errors of index modulation. Therefore, the optimum configurations of DSA-OFDM under the constraints of illumination and spectral efficiency can be obtained as

$$\max_{N_A,K} \text{SNR} \tag{21}$$

$$\text{s.t.} \quad \eta = \frac{N_A\,(B_{\mathrm{L}} - I_{\mathrm{L}})}{N_T\,(I_{\mathrm{H}} - I_{\mathrm{L}})} \times 100\%, \tag{21a}$$

$$\xi = \frac{N_f - 2N}{2NN_f}\left(K\log_2(M) + \left\lfloor \log_2\binom{N}{K} \right\rfloor\right) + \left\lfloor \log_2\binom{N_T}{N_A} \right\rfloor, \tag{21b}$$

$$\alpha \geq 0. \tag{21c}$$

Since σ^2_{index} is further affected by σ_z^2 and σ_w^2, there is a complex relationship among σ_z^2, σ_w^2 and σ^2_{index}. Therefore, it is challenging to present the closed-form expressions of σ^2_{index}, and then we solve problem (21) by simulations.

4. Numerical and Simulation Results

In this section, numerical and simulation results are presented to evaluate the performance of the proposed DSA-OFDM scheme. In addition, three baseline schemes, SD-OFDM, DCO-OFDM with index modulation (DCO-OFDM-IM) and HD-OFDM, are also simulated for comparisons. In this work, an avalanche photodiode (ThorLabs unit (#APD120A2)) positioned on a servo is assumed, and with the help of the lens mounted on the receiver surface, the value of $\Psi_{1/2}$ can be adjusted from 20° to 90° [33]. To ensure that the PD can receive signals from multiple LEDs, $\Psi_{1/2} = 80^\circ$ is set in this work. Unless otherwise specified, the main system parameters are shown in Table 2.

The CCDFs of PAPR in DSA-OFDM having different values of K/N are shown in Fig. 4, in which the theoretical and simulation results are plotted. We can observe that the theoretical results match well with the simulation results. Furthermore, the PAPR of DSA-OFDM increases with K/N. This is due to the fact that, according to (13), the PAPR increases when there are more activated subcarriers in a subblock. In particular, the PAPR of DSA-OFDM with $K/N = 0.5$ achieves 3 dB performance gain when compared with classical D-OFDM (i.e. when $K/N = 1$) at a CCDF level of 10^{-3}.

We define $\Upsilon \triangleq 10\log_{10}(c^2 + 1)$ dB to represent the magnitude of the electrical power of time domain signals u_n, where $c = \min(I_{\mathrm{H}} - B_{\mathrm{L}}, B_{\mathrm{L}} - I_{\mathrm{L}})/\alpha$ [34]. As shown in Fig. 5, both the simulation and the theoretical results of the clipping noise are plotted to verify the accuracy of our analysis. It can be observed that the theoretical results match well with the simulation results when the value of Υ is large. However, when Υ is small (i.e. the clipping noise is severe), some deviation is shown due to the Gaussian approximation [15]. Meanwhile, the clipping noise of DSA-OFDM

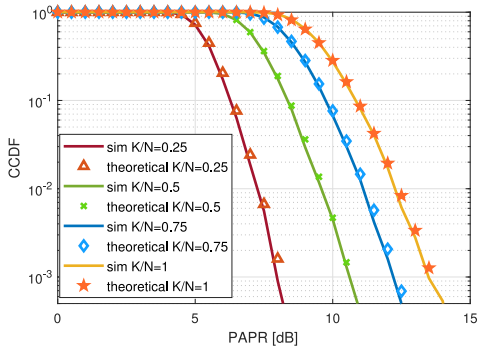

Fig. 4. CCDFs of PAPR in DSA-OFDM with different K/N.

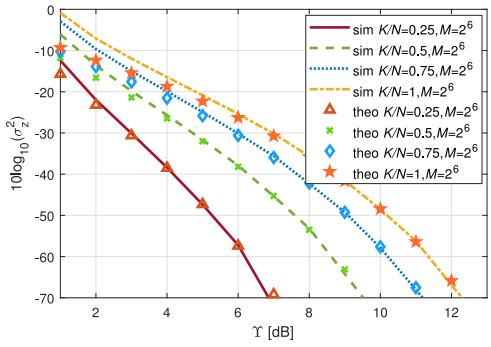

Fig. 5. The clipping noise of DSA-OFDM with different K/N.

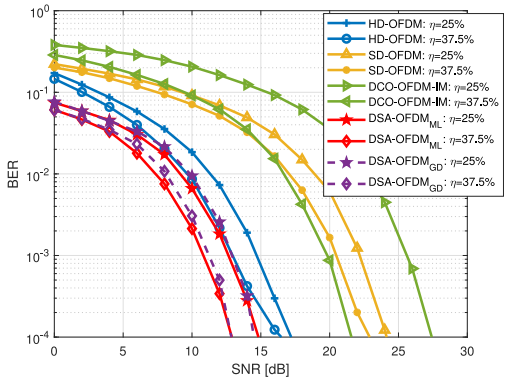

Fig. 6. The BER performance comparison among DSA-OFDM and its counterparts when the illumination level is 25% and 37.5%.

increases with K/N. Note that the number of activated subcarriers can be adjusted in DSA-OFDM, and provides one more dimension for performance optimization in existing D-OFDM schemes. In particular, HD-OFDM is the special case of DSA-OFDM for $K/N = 1$. Thus, it can be observed that compared with HD-OFDM, the DSA-OFDM has less clipping noise due to the lower PAPR.

The BER performance of DSA-OFDM is compared with that of SD-OFDM, DCO-OFDM-IM and HD-OFDM in Fig. 6 and Fig. 7. For fair comparisons, we have set the same lower SE bound 3 bit/s/Hz for all these schemes and all the schemes in Fig. 6 and Fig. 7 are optimized. In particular, for given η and ξ, the number of activated subcarriers and DC bias are optimized in DCO-OFDM-IM;

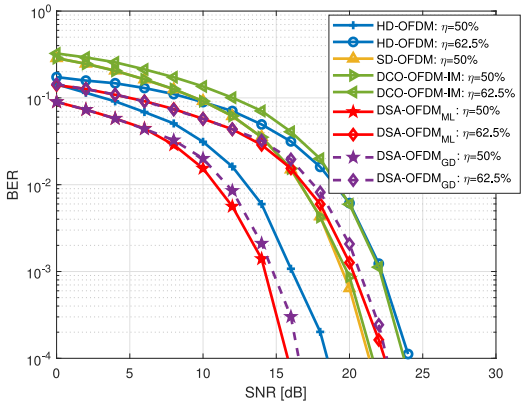

Fig. 7. The BER performance comparison among DSA-OFDM and its counterparts when the illumination level is 50% and 62.5%.

the number of activated LEDs and DC bias are optimized in HD-OFDM; and the number of activated LEDs is optimized to $N_A = \left\langle \frac{\eta N_T}{\eta_e} \right\rangle$ in SD-OFDM, where $\langle \cdot \rangle$ denotes the rounding function. However, since the optimum configuration varies with the SNRs in DSA-OFDM and its counterparts, the actual SEs of these schemes are dynamic. It can be observed that the DSA-OFDM with ML or GD detector can always obtain performance gains at different illumination levels compared with the other three D-OFDM schemes. For example, when the illumination level is 25%, DSA-OFDM achieves 2 dB, 8 dB and 6 dB performance gains compared with HD-OFDM, SD-OFDM and DCO-OFDM-IM at a BER of 10^{-4}, respectively. Besides, when the illumination level is 62.5%, DSA-OFDM achieves 1 dB BER gains compared with both HD-OFDM and DCO-OFDM-IM. Moreover, it is can be observed from Fig. 6 and Fig. 7 that the BER performance of GD detector approaches that of ML detector. Please note all SD-OFDM has a fixed DC bias at the middle of the dynamic range of LEDs [9], and therefore in terms of the definition given in (4), the maximum illumination level of SD-OFDM is only 50%.

5. Conclusion

This work proposed a DSA-OFDM scheme to mitigate the contradiction between the high PAPR of OFDM signals and the limited dynamic range of LEDs. Different from the existing D-OFDM schemes, frequency domain design is incorporated for dimming control such that the number of activated subcarriers, as well as the signal's DC bias and the number of activated LEDs, is adjusted for a target illumination level. In addition, a generalized index modulation in both spatial domain and frequency domain is designed to select the indices of activated subcarriers and activated LEDs. The analytical expressions of the PAPR and the clipping noise of the proposed scheme were derived, and the optimized signal form of DSA-OFDM is obtained accordingly. Simulation and numerical results verified that both the PAPR and the clipping noise of DSA-OFDM are lower than that of typical D-OFDM schemes, and thus DSA-OFDM can outperform conventional dimming control schemes at various illumination levels in terms of the BER performance. In our future work, we will further build a prototype and experimentally to verify the efficiency of DSA-OFDM.

References

[1] M. S. Islim, D. Tsonev, and H. Haas, "Spectrally enhanced PAM-DMT for IM/DD optical wireless communications," in *Proc. IEEE 19th Int. Symp. Pers., Indoor Mobile Radio Commun.*, 2015, pp. 877–882.

[2] M. Chen, M. Mozaffari, W. Saad, C. Yin, M. Debbah, and C. S. Hong, "Caching in the sky: Proactive deployment of cache-enabled unmanned aerial vehicles for optimized quality-of-experience," *IEEE J. Sel. Areas Commun.*, vol. 35, no. 5, pp. 1046–1061, May 2017.

[3] H. Zhang, N. Liu, K. Long, J. Cheng, V. C. M. Leung, and L. Hanzo, "Energy efficient subchannel and power allocation for software-degined heterogeneous VLC and RF networks," *IEEE J. Sel. Areas Commun.*, vol. 36, no. 3, pp. 658–670, Mar. 2018.

[4] A. I. Siddiq, "Effect of subcarrier activation ratio on the performance of OFDM-IM over Rayleigh fading channel," *IEEE Commun. Lett.*, vol. 21, no. 6, pp. 1293–1296, Jun. 2017.

[5] R. Islam, P. Choudhury, and M. A. Islam, "Analysis of DCO-OFDM and flip-OFDM for IM/DD optical-wireless system," in *Proc. 8th Int. Conf. Elect. Comput. Eng.*, 2014, pp. 32–35.

[6] J. Armstrong and A. J. Lowery, "Power efficient optical OFDM," *Electron Lett.*, vol. 42, no. 6, pp. 370–372, Mar. 2006.

[7] Y. Yang, Z. Zeng, J. Cheng, and C. Guo, "An enhanced DCO-OFDM scheme for dimming control in visible light communication systems," *IEEE Photon. J.*, vol. 8, no. 3, Jun. 2016, Art. no. 7904813.

[8] H. Elgala and T. D. C. Little, "Reverse polarity optical-OFDM (RPO-OFDM): Dimming compatible OFDM for gigabit VLC links," *Opt. Exp.*, vol. 21, no. 20, pp. 24288–24299, Oct. 2017.

[9] Y. Yang, Z. Zeng, J. Cheng, and C. Guo, "Spatial dimming scheme for optical OFDM based visible light communication," *Opt. Express*, vol. 24, no. 26, pp. 30254–30263, Dec. 2016.

[10] Y. Yang, Z. Zeng, J. Cheng, and C. Guo, "A novel hybrid dimming control scheme for visible light communications," *IEEE Photon. J.*, vol. 9, no. 6, Dec. 2017, Art. no. 7908312.

[11] S. Han and J. Lee, "An overview of peak-to-average power ratio reduction techniques for multicarrier transmission," *IEEE Wireless Commun.*, vol. 12, no. 5, pp. 56–65, Apr. 2005.

[12] W. O. Popoola, Z. Ghassemlooy, and B. G. Stewart, "Pilot-assisted PAPR reduction technique for optical OFDM communication systems," *J. Lightw. Technol.*, vol. 32, no. 7, pp. 1374–1382, Apr. 2014.

[13] K. Bandara, P. Niroopan, and Y.-H. Chung, "PAPR reduced OFDM visible light communication using exponential nonlinear companding," in *Proc. IEEE Int. Conf. Microw. Commun. Antennas Electron. Syst.*, 2013, pp. 1–5.

[14] H. Zhang, Y. Yuan, and W. Xu, "PAPR reduction for DCO-OFDM visible light communications via semidefinite relaxation," *IEEE Photon. Technol. Lett.*, vol. 26, no. 17, pp. 1718–1721, Sep. 2014.

[15] M. S. A. Mossaad, S. Hranilovic, and L. Lampe, "Visible light communications using OFDM and multiple LEDs," *IEEE Trans. Commun.*, vol. 63, no. 11, pp. 4304–4313, Nov. 2015.

[16] H. Dong, H. Zhang, K. Lang, B. Yu, and M. Yao, "OFDM visible light communication transmitter based on LED array," *Chin. Opt. Lett.*, vol. 12, no. 5, pp. 1–4, May 2014.

[17] Z. Wu, C. You, C. Yang, L. Liu, K. Xuan, and J. Wang, "Research on long-range real-time visible light communications over phosphorescent LEDs," in *Proc. Chin. Control Decis. Conf.*, 2017, pp. 5838–5842.

[18] C. H. Yeh, C. W. Chow, H. Y. Chen, Y. L. Liu, and D. Z. Hsu, "Investigation of phosphor-LED lamp for real-time half-duplex wireless VLC system," *J. Opt.*, vol. 18, no. 6, pp. 1–6, Apr. 2016.

[19] X. Huang *et al.*, "2.0-Gb/s visible light link based on adaptive bit allocation OFDM of a single phosphorescent white LED," *IEEE Photon. J.*, vol. 7, no. 5, Oct. 2015, Art. no. 7904008.

[20] S. Dimitrov and H. Haas, "Information rate of OFDM-based optical wireless communication systems with nonlinear distortion," *J. Lightw. Technol.*, vol. 31, no. 6, pp. 918–929, Mar. 2013.

[21] T. Komine and M. Nakagawa, "Fundamental analysis for visible-light communication system using LED lights," *IEEE Trans. Consum. Electron.*, vol. 50, no. 1, pp. 100–107, Feb. 2004.

[22] G. Ntogari, T. Kamalakis, J. Walewski, and T. Sphicopoulos, "Combining illumination dimming based on pulse-width modulation with visible-light communications based on discrete multitone," *IEEE J. Opt. Commun. Netw.*, vol. 3, no. 1, pp. 56–65, Mar. 2011.

[23] Z. Wang, "Performance of dimming control scheme in visible light communication system," *Opt. Express*, vol. 20, no. 17, pp. 18861–18868, Aug. 2012.

[24] O. Sayl, H. Dogan, and E. Panayirci, "On channel estimation in DC biased optical OFDM systems over VLC channels," in *Proc. Int. Conf. Adv. Technol. Commun.*, 2016, pp. 147–151.

[25] H. Ochiai and H. Imai, "On the distribution of the peak-to-average power ratio in OFDM signals," *IEEE Trans. Commun.*, vol. 49, no. 2, pp. 282–289, Feb. 2001.

[26] Z. Yu, R. J. Baxley, and G. T. Zhou, "Distributions of upper PAPR and lower PAPR of OFDM signals in visible light communications," in *Proc. IEEE Int. Conf. Acoust., Speech Signal Process.*, 2014, pp. 355–359.

[27] E. Basar, "Multiple-input multiple-output OFDM with index modulation," *IEEE Signal Process. Lett.*, vol. 22, no. 12, pp. 2259–2263, Dec. 2015.

[28] E. Basar, "On multiple-input multiple-output OFDM with index modulation for next generation wireless networks," *IEEE Trans. Signal Process*, vol. 64, no. 15, pp. 3868–3878, Aug. 2016.

[29] R. Rajashekar, K. V. S. Hari, and L. Hanzo, "Reduced-complexity ML detection and capacity-optimized training for spatial modulation systems," *IEEE Trans. Commun.*, vol. 62, no. 1, pp. 112–125, Jan. 2014.

[30] H. Yu, M. Chen, and G. Wei, "Distribution of PAR in DMT systems," *Electron. Lett.*, vol. 39, no. 10, pp. 799–801, May 2003.

[31] Z. Yu, R. J. Baxley, and G. T. Zhou, "Distributions of upper PAPR and lower PAPR of OFDM signals in visible light communications," in *Proc. IEEE Int. Conf. Acoust., Speech Signal Process.*, 2014, pp. 355–359.

[32] E. Basar and E. Panayirc, "Optical OFDM with index modulation for visible light communication," in *Proc. 4th Int. Workshop Opt. Wireless Commun.*, 2015, pp. 11–15.

[33] I. Abdalla, M. Rahaim, and T. Little, "Impact of receiver FOV and orientation on dense optical networks," in *Proc. IEEE Global Commun. Conf.*, 2018, Art. no. 18472491.

[34] J. Armstrong and B. J. C. Schmidt, "Comparison of asymmetrically clipped optical OFDM and DC-biased optical OFDM in AWGN," *IEEE Commun. Lett.*, vol. 12, no. 5, pp. 343–345, May 2008.